3

Radio counterpart of the lensed sub-mm emission SMM J04542−0301

Previous authors have reported the detection of intrinsically faint sub-mm emission lensed by the cluster MS0451.6−0305. They suggest that this emission arises from a merging system composed of a Ly-break galaxy and a pair of extremely red objects which are multiply-imaged in the optical/NIR observations. Since the sub-mm emission presents an unusually large angular extent (∼1′), the possible radio emission associated with that system can help to identify optical/NIR counterparts due to the higher spatial resolution and astrometric accuracy of the radio observations. We present a radio map of the central region of MS0451.6−0305 produced using VLA archival data (BnA configuration at 1.4 GHz), and report the detection of gravitationally lensed radio emission coincident with the previously discovered sub-mm lensed emission. The overall morphology and scale of the radio and sub-mm emission are strikingly similar. This observation strongly suggests that the radio and sub-mm emission arise from the same sources. Preliminary estimates of the total $S_{850\mu m}/S_{1.4GHz}$ flux density ratio appear to be consistent with that expected from distant star forming galaxies. The radio emission is resolved into 7 distinct components, and the overall structure can be explained, using a simple lens model, with three multiply-imaged radio sources at z ∼ 2.9. One of these sources is predicted to lie in the middle of the previously mentioned merger system in the source plane, suggesting that it is related to the intense star formation generated during the merging process.

Originally published as:
A. Berciano Alba, M.A. Garrett, L.V.E. Koopmans, & O. Wucknitz, 2007, A&A, vol. 462, p.903

3.1 Introduction

Sub-mm galaxies (SMGs) were first detected by SCUBA[1] (Smail et al. 1997) and are believed to be dusty star forming galaxies located at high redshift (e.g. Ivison et al. 2002; Smail et al. 2002; Chapman et al. 2003). It is also suggested that they are the progenitors of present-day massive elliptical galaxies (e.g. Lilly et al. 1999; Swinbank et al. 2006b). Little is known about the objects associated with the faint end of the SMG population ($S_{850\mu m} < 2$mJy), but they are predicted to dominate (energetically) the population as a whole (Knudsen 2004). A recent statistical stacking analysis (Knudsen et al. 2005), suggests that distant red galaxies (DRGs) and Extremely Red Objects (EROs) contribute $\sim 50\%$ of the flux density of sub-mm sources with $0.5 < S_{850\mu m} < 5$mJy.

Intrinsically faint SMG cannot easily be detected, since their flux densities lie below the ~ 2 mJy confusion limit of SCUBA images at 850 μm. Typically they also fall well below the (thermally limited) sensitivity of current radio instruments, such as the VLA. Individual systems can often only be detected via strong gravitational lensing effects, produced by massive foreground clusters of galaxies (Knudsen 2004; Kneib et al. 2004b; Garrett et al. 2005). The spatial magnification provided by the lensing cluster overcomes instrumental confusion limitations in the sub-mm and also boosts the measured flux density of the source (provided the lensed images remain unresolved), thereby increasing the probability of detection (Blain 1997). Another advantage of cluster lensing is that the magnification provided by the lens effectively increases the spatial resolution of the observations, with the largest magnifications usually occurring in cases of multiple imaging. SMM J16359+6612, associated with the cluster Abell 2218, was the first intrinsically faint, multiply imaged SMG detected in both the sub-mm (Kneib et al. 2004b) and radio (Garrett et al. 2005). In this Chapter, we present VLA 1.4 GHz radio observations of a second case, SMM J04542−0301 (Chapman et al. 2002a), associated with the cluster MS0451.6−0305.

MS0451.6−0305 is a cluster of galaxies situated at z = 0.55 (Gioia & Luppino 1994) that has recently been observed in optical and near-Infrared (NIR) (Borys et al. 2004a). The analysis of these observations indicate that the sub-mm emission is probably originating from an interacting system of three objects lying at $z \sim 2.9$: a Lyman Break Galaxy (LBG) and a pair of Extremely Red Objects (EROs). The LBG is imaged into two visible arcs, and the ERO pair is supposed to be associated with 5 NIR sources located within the sub-mm emission (Takata et al. 2003; Borys et al. 2004a, T03 and B04 hereafter). However, the emission coming from the north-eastern and the central regions of the sub-mm image do not seems to be associated with the LBG and the ERO pair (see Fig. 7 from B04).

In this Chapter, we present deep, high resolution 1.4 GHz VLA observations of SMM J04542−0301. In Sect. 3.2, we describe the VLA data analysis and present the resultant radio images. Section 3.3 describes a simple lens model for the system, in an attempt to explain the lensed nature of the radio emission related to SMM J04542−0301. In Sect. 3.4, we compare the radio and sub-mm emission, including a discussion about possible optical/NIR counterparts, and the preliminary calculation

[1]Sub-millimeter Common-User Bolometer Array, mounted at the James Clerk Maxwell Telescope (JCMT)

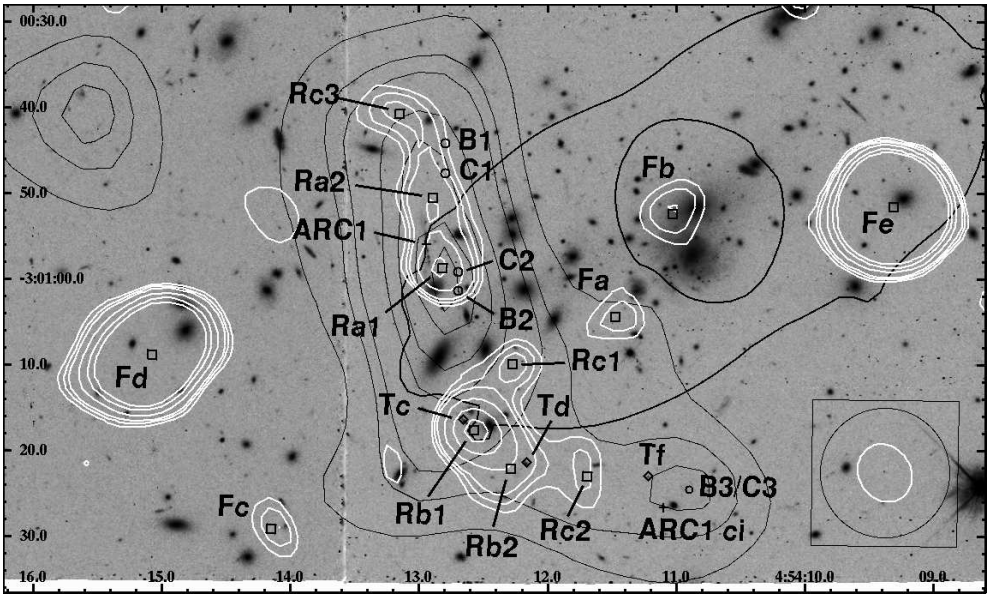

Figure 3.1: *The VLA 1.4 GHz naturally weighted contour map (solid white lines) superimposed upon the SCUBA 850-μm contour map (solid thin black lines) and a HST F702W image of the centre of the cluster MS0451.6−0305 (Borys et al. 2004a). The axes represent the right ascension (x-axis) and declination (y-axis) in the J2000 coordinate system. The solid thick black curves are the tangential (outer) and radial (inner) critical lines at* $z = 2.911$ *associated with the lens model of the cluster determined by Borys et al. (2004a). The boxes indicate the positions obtained via Gaussian fits of the radio sources. The diamonds correspond to the positions of three EROs from Takata et al. (2003), and the crosses/circles are the positions of a LBG lensed as two arc (*ARC1 *and* ARC1 ci*), and a triply-imaged EROs pair:* B1/B2/B3 *(images of ERO B) and* C1/C2/C3 *(images of ERO C) (see Borys et al. 2004a). The squares and circles have a size of 1″ to illustrate the random and systematic errors due to measurement uncertainties and the alignment of the different images. Contours of the* radio map *are drawn at -3, 3, 4, 5, 8, 12 & 16 times the 1σ noise level of 9 μJy beam^{-1}. Contours of the* sub-mm map *are drawn at 4, 6, 7, 9, 10, 11 & 11.5 mJy beam^{-1}. The white circle inside a box in the bottom-right corner is the beam size of the radio map (*$6.99'' \times 6.03''$ *in position angle* PA $= 32.6°$*) whereas the black one corresponds to the beam size of the sub-mm map (*$15'' \times 15''$*).*

of the $S_{850\mu\mathrm{m}}/S_{1.4\mathrm{GHz}}$ flux density ratio. A summary of our main results is presented in Sect. 3.5. In the following discussion, we assume a ΛCDM cosmological model with Ω_m=0.3 , Ω_λ=0.7 and h_0=0.7.

3.2 Radio Observations

VLA 1.4 GHz observations of the cluster MS0451.6−0305, made in June 2002, were retrieved from the NRAO[2] data archive system[3]. The integration time was 7.8 hours with the VLA in BnA configuration, employing two 25 MHz IFs in both left and right-hand circular polarization. Each IF was subdivided into 7 channels. The data analysis was performed using the NRAO AIPS package using standard analysis techniques. The absolute flux density scale was set by observations of 0137+331, and phase calibration was performed via short observations of 0503+020 between the 1 hour target scans. A wide-field image was made and bright sources far from the field centre were subtracted from the data. Self-calibration using the remaining sources in the centre of the field realised images with a 1σ rms noise level of 9 μJy beam^{-1}.

In Fig. 3.1, we present the radio contour map (solid white lines) of the naturally weighted VLA image of SMM J04542−0301, superimposed upon the HST F702W image and the sub-mm contour map (solid thin black lines) presented in B04. Note that the SCUBA beam is 15″ × 15″, significantly larger than the VLA beam (6.99″ × 6.03″). To compare the radio and sub-mm emission at the same resolution (see Sect. 3.4), we also produced a tapered image of the radio data, weighting down the long baselines to reach a Gaussian restoring beam similar to the SCUBA beam. The resulting map is presented in Fig. 3.3 (solid white lines).

The AIPS task IMFIT was used to fit Gaussian components to all the radio sources detected in the field (3 and 4 Gaussians simultaneously, in the case of the two extended regions of radio emission in the naturally weighted map). The resultant radio positions are indicated with square boxes in Fig. 3.1. The results are listed in Table 3.1, together with their formal errors.

The radio sources *Ra*, *Rb*, *Rc* and *Fa* appear to be related to the sub-mm emission. The source *Fb* may be related to the central brightest cluster galaxy (BCG) (see Table 3.6), but there is no obvious optical/NIR counterpart for *Fc*.

We also detect two strong radio sources (*Fd* and *Fe*) which are almost two orders of magnitude brighter than the other radio sources in the field. The latter is clearly identified with a optical/NIR counterpart. These sources are probably not lensed images of the same background source — *Fe* is more compact than *Fd*, even though it is brighter. The positions of *Fd* and *Fe* are coincident (within the errors) with two radio sources already reported in Stocke et al. (1999) (see Table 3.6).

3.3 A lens model of the radio emission

In order to aid our interpretation of the radio emission associated with SMM J04542−0301, we have created a simple elliptical lens model with external shear to describe the cluster lens potential. Our analysis employs the GRAVLENS software package developed by Keeton (2001). The modeling strategy is described in Sect. 3.3.1, and the results of the model are discussed in Sect. 3.3.2.

[2]National Radio Astronomy Observatory.
[3]project ID AN0109, PI: Nakanishi.

Table 3.1: ***Details of the radio sources observed in the core of MS0451.6−0305****. The columns show: position (RA, DEC), peak flux density (S_{Pk}), total flux density (S_T) and deconvolved Gaussian sizes (major axis, minor axis and position angle) with their corresponding formal errors. Cases where the parameters of the Gaussian fits are not well constrained are indicated by a dash. The coordinates are given as offsets with respect to the cluster centre,* RA(J2000) = $4^h54^m10.8^s$, DEC(J2000) = −3°0′51.6″ *(see Takata et al. 2003, Table 2).*

Name	RA J2000 (″)	DEC J2000 (″)	S_{Pk} μJy	S_T μJy	Maj Axis (″)	Min Axis (″)	PA deg
Ra2	31.3±0.3	1.1 ± 0.4	70 ± 8	95 ± 18	6 ± 1	2 ± 1	27 ± 28
Ra1	30.3±0.2	−7.1 ± 0.2	109 ± 9	109 ± 9	–	–	–
Rb1	26.5±0.2	−26 ± 0.2	151 ± 9	151 ± 9	–	–	–
Rb2	22.3±0.5	−30.50 ± 0.7	52 ± 8	100 ± 22	9 ± 2	3 ± 2	158 ± 14
Rc1	22.1±0.6	−18.3 ± 0.4	50 ± 9	55 ± 16	6 ± 2	–	112 ± 11
Rc2	13.5±0.6	−31.3 ± 0.8	41 ± 8	58 ± 18	7 ± 2	1 ± 3	10 ± 163
Rc3	35.4±0.8	10.9 ± 0.5	52 ± 8	78 ± 19	8 ± 2	0 ± 2	73 ± 11
Fa	10.1±0.6	−12.7 ± 0.6	45 ± 9	50 ± 17	4 ± 6	0 ± 4	123 ± 38
Fb	3.5 ±0.6	−0.8 ± 0.6	49 ± 9	70 ± 20	6 ± 5	3 ± 6	122 ± 45
Fc	50.4±0.6	−37.5 ± 0.6	44 ± 9	44 ± 9	–	–	–
Fd	64.1±0.1	−17.2 ± 0.1	634 ± 9	1039 ± 21	7.6 ± 0.1	1.4 ± 0.5	128 ± 1
Fe	−22.40±0.02	−0.07 ± 0.02	1549 ± 9	1777 ± 17	3.3 ± 0.1	0.8 ± 0.5	125 ± 3

3.3.1 Modeling strategy

The first lens model of MS0451.6−0305 was presented in T03, and describes the total mass distribution of the cluster by a singular isothermal ellipsoid. To be more sensitive to the local mass distribution, B04 modeled the cluster core and 39 galaxy cluster members using 40 smoothly truncated pseudo-isothermal elliptical mass distribution profiles (PIEMD, see Kneib et al. 1996).

The critical curves of the best lens model found by B04 are shown in Fig. 3.1. It can be seen that the tangential critical curve lies between the radio emission *Ra1-Ra2*, *Rb1-Rb2* and *Rc1-Rc2*. Based on the general properties of the lens geometry, this suggests that each of these image pairs belongs to a group of 3 images produced by one source located close to the caustic in the source plane. In order to explain the distribution of radio sources, we propose the following scenario:

- *Ra2-Ra1* are fold images of a source *Ra*, with an expected counterpart image (*Ra3*) close to *ARC1ci*.
- *Rb1-Rb2* are fold images of a source *Rb* with an expected counterpart image (*Rb3*) close to *Rc3*.
- *Rc1-Rc2-Rc3* are multiple images of a single source *Rc*, located behind the cluster.

To test this hypothesis, we implemented a new lens model for MS0451.6−0305 using the GRAVLENS code. Since we are only interested in testing the lensed nature of the radio emission, we modeled the overall mass distribution of the cluster using a single mass profile plus external shear (see Appendix 1 for details). Unlike the

Table 3.2: ***Optical/NIR constraints used in the lens model***. *The columns show: position (RA, DEC), total flux density in K′ band and predicted magnification μ (see also Table 1 in B04). The coordinates are given as offsets with respect to the cluster centre,* RA(J2000) = $4^h54^m10.8^s$, DEC(J2000) = $-3°0'51.6''$ *(see Takata et al. 2003, Table 2).*

Name	RA J2000 ($''$)	DEC J2000 ($''$)	Flux in K′ band μJy	μ
B1	29.95	7.498	3.6 ± 0.1	8 ± 1
B2	28.47	−9.702	1.9 ± 0.1	10 ± 1
C1	29.95	4	1.4 ± 0.1	10 ± 1
C2	28.47	−7.502	0.9 ± 0.1	5 ± 1
B3/C3	1.481	−32.9	2.5 ± 0.1	5 ± 1

two previous models, we choose an NFW profile (Navarro et al. 1996) for the cluster mass distribution that is consistent with observations (e.g. Pointecouteau et al. 2005; Comerford et al. 2006; Bassino et al. 2006) and predictions from dark matter simulations.

To constrain the model, we performed a number of distinct steps. First, the parameters of the mass model were chosen in order to reproduce the general shape of the critical lines determined by B04 (see Fig. 3.1). Second, the positions and fluxes of the ERO images (*B1*, *C1*, *B2*, *C2*, *B3/C3*) were used as constraints for the first optimization of the input model. And third, we included the positions and fluxes of the radio images as new constraints (following the previous hypothesis) to re-optimize the model. The constraints are listed in Tables 3.1 and 3.2. The coordinates of the cluster centre used in T03 were chosen as the origin of the coordinate system.

The lens model obtained through this process turned out to have a degeneracy between the mass and the scale radius. To break this degeneracy, we used information about the concentration parameter (δ_c) derived from ΛCDM N-body simulations. First, we produced a set of 10 new models varying the core radius between 40 and 150 (a range that contains the core radius value of the degenerate model). Following the formalism presented in Bullock et al. (2001), we calculated the concentration parameter and the virial mass for the set of new models (see Appendix 1 for details). We found that, while δ_c varies between 3.3 and 9.6, the virial mass is always of the order of $10^{15}M_\odot$. For a halo of that mass situated at z = 0.55, the toy model presented in Bullock et al. (2001) predicts a concentration parameter of $\delta_c = 3.35$. So we plotted δ_c versus the core radius for the set of new models, interpolating the results in order to determine the core radius that corresponds to $\delta_c = 3.35$. Finally, we fixed the core radius of the model to this value and re-optimized the remaining parameters.

3.3.2 Results

Figure 3.2 and Table 3.3 show the results of the lens model. Although the model is not unique, it is able to reproduce the positions of the ERO images and the radio emission (*Ra1*, *Ra2*, *Rb1*, and *Rb2*) very well. The largest offsets are found for *Rc1*,

Table 3.3: ***Lens model results***. *The columns show: coordinates of the predicted images (RA, DEC), predicted lensed flux (S_T), offsets between the measured and predicted quantities (ΔRA, ΔDEC, ΔS_T) and predicted magnification (μ). The coordinates are given as offsets with respect to the cluster centre,* RA(J2000) = $4^h54^m10.8^s$, DEC(J2000) = $-3°0'51.6''$ *(see Takata et al. 2003, Table 2).*

Name	RA ('')	ΔRA ('')	DEC ('')	ΔDEC ('')	S_T μJy	ΔS_T μJy	μ
B1	−29.80	−0.15	7.25	−2.75	2.82	0.75	12.19
B2	−28.05	−0.42	−9.76	0.06	2.70	0.83	−11.66
B3	−1.50	0.02	−32.66	−0.24	1.13	0.11	4.89
C1	−30.07	0.12	4.23	−0.23	1.31	0.11	17.66
C2	−28.92	0.45	−7.40	−0.1	1.26	0.36	−17.00
C3	−1.47	−0.01	−33.14	0.24	0.35	0.88	4.75
Ra2	−31.03	−0.29	0.94	0.17	100.95	−5.95	25.18
Ra1	−29.99	−0.26	−7.18	0.12	99.23	−9.77	−24.76
Ra3	−3.30	–	−33.67	–	19.73	–	4.92
Rb1	−26.75	0.23	−26.52	0.54	131.12	−19.88	−36.78
Rb2	−22.11	−0.22	−30.70	0.2	111.05	−11.05	31.15
Rb3	−36.93	–	−2.58	–	37.65	–	10.56
Rc1	−24.16	2.11	−22.12	3.86	72.17	17.17	−11.51
Rc2	−11.76	−1.76	−30.90	−0.43	62.34	−4.34	9.94
Rc3	−32.96	−2.39	10.28	0.63	42.37	35.63	6.75

Rc2 and *Rc3* (see panel 4 in Fig. 3.2) which are the most distant images from the critical curves. This is consistent with the effect of degeneracies in the global mass model near the critical curves: a change in the model parameters produces a more significant change in the image properties when they are located further from the critical curves.

To improve the fit of images *Rc1-Rc2-Rc3*, the redshift of the model was changed for source *Rc*, but this only produces a radial shift of their predicted positions *in the same direction*, something that cannot improve the fit shown in panel 4. Therefore, we believe that the most important contribution to this offset is probably coming from the group of galaxies in the region between *Ra1* and *Rc1* (see Fig. 3.1). This group of galaxies is expected to introduce perturbations in the overall mass distribution of the cluster which are not accounted for in the smooth NFW mass model.

One notable result is that the model predicts two faint counterpart images (*Ra3* and *Rb3*) that do not appear in our radio image. In our model *Ra3* and *Rb3* are less magnified than *Ra1-Ra2* and *Rb1-Rb2* respectively. The predicted relative magnifications suggest that *Ra3* and *Rb3* should appear in our maps at the 2 and 4σ level respectively, but there is no evidence for this in the radio images. We note, however, that the predicted magnifications depend strongly on the overall mass model employed and perturbations by individual galaxies, so they should be treated as rough

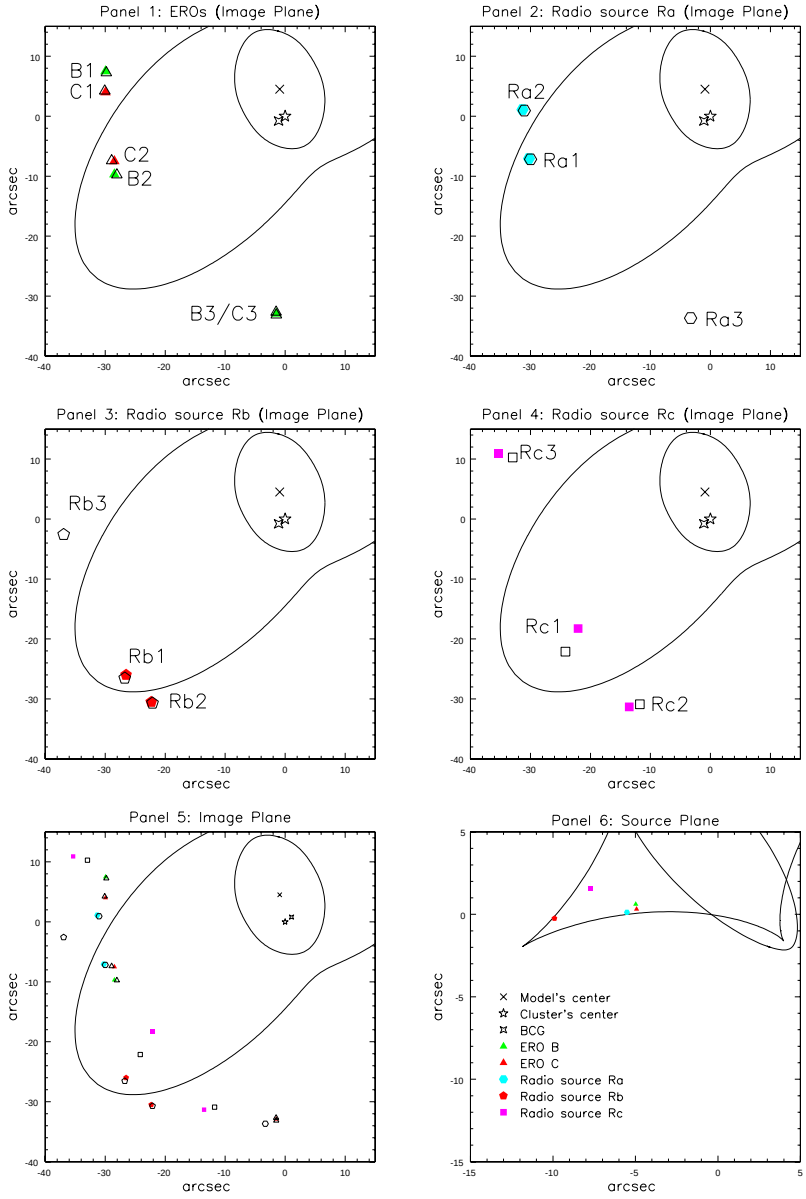

Figure 3.2: ***Lens model results.*** *The solid black curves represent the critical curves (panels 1 - 5) and caustics (panel 6) that define the model. Filled symbols represent the measured positions of the ERO images (Borys et al. 2004a) and the radio components; empty symbols are the positions predicted by the model. The ERO pair and each group of suggested multiply-imaged radio components are shown separately in different panels (1 to 4). Panel 5 shows all of these components plotted together. Panel 6 shows the position of the ERO pair and radio sources in the source plane.*

Table 3.4: ***Lens model parameters.*** *The columns show: Mass model (Model), Mass scale (κ_s), Galaxy position in arcsec (x_0, y_0), ellipticity (e, θ_e), external shear (γ, θ_γ) and scale radius in arcsec (r_s). The errors represent the 1σ level of the χ^2 function for each parameter. The scale radius has no error estimations because its value was fixed during the optimization process to be consistent with a concentration parameter of 3.35 (see sect.3.3.1)*

Model	κ_s	x_0	y_0	e	θ_e	γ	θ_γ	r_s
NFW	$0.33^{+0.01}_{-0.01}$	$-0.90^{+0.7}_{-1.2}$	$4.51^{+0.9}_{-1.4}$	$0.55^{+0.03}_{-0.03}$	$-42.20^{+1.1}_{-5.6}$	$0.18^{+0.02}_{-0.02}$	$61.44^{+2.4}_{-8.4}$	[142.90]

estimates of the true magnification. Therefore, the non-detection of these images do not necessarily mean that the lens model is wrong, since the real magnification could be less than that predicted by this simple model.

The mass model parameters that characterise the NFW profile are summarised in Table 3.4. The errors represent the 1σ level of the χ^2 function of each parameter. We note that the shear of the model is quite large, and the model centre is shifted ΔRA = $-0.9''$ and ΔDEC = $4.5''$ from the assumed position of the cluster centre. These effects are most likely systematic errors that compensate for the contribution of the group of galaxies that we are not including in the model, and the fact that we are forcing it to fit *Rb1* and *Rb2* as mirror images (a hypothesis that we will discuss in detail in Sect. 3.4).

As already noted, this lens model is only meant to test if the configuration of the observed radio emission can be understood as the result of gravitational lensing. In that sense, Fig. 3.2 shows that the model is able to reproduce the position of the EROs and the radio observations reasonably well, explaining the morphology of the radio map as the result of three lensed background radio sources. Therefore, we expect the two EROs and the three radio sources lie at the same redshift in the source plane ($z \sim 2.9$, estimated in B04 for the EROs including the spectroscopic redshift information of the ARC in their lens model).

But perhaps the most interesting result from the lens model is that the source *Ra* and the EROs *B* and *C* are predicted to be located inside a region of about 0.6''in the source plane (see panel 6 of Fig. 3.2), which corresponds to a linear separation of only 4.7 kpc. The same situation is found in the case of the LBG and the ERO pair, which are separated by ~10 kpc in the source plane (see B04). This means that the radio source *Ra* is lying just between the LBG and the EROs, all of which are located in a region smaller than the extent of a typical galaxy (~20 kpc). It would appear therefore, that the radio source *Ra*, the LBG and the ERO pair indeed constitute an interacting or merging system of galaxies.

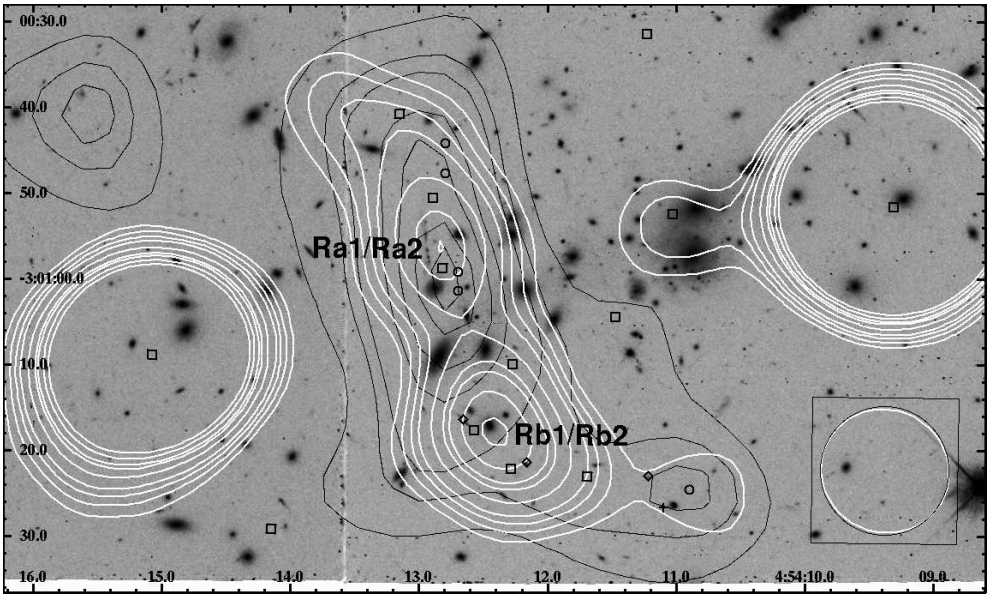

Figure 3.3: *The VLA 1.36 GHz tapered contour map (solid white lines) superimposed upon the SCUBA 850-μm contour map (solid black lines) and a HST F702W image of the centre of the cluster MS0451.6−0305 (Borys et al. 2004a). The axes represent the right ascension (x-axis) and declination (y-axis) in the J2000 coordinate system. Contours of the* tapered radio map *are drawn at -3, 3, 4, 5, 6, 8, 10, 11, 13 & 15 times the 1σ noise level of 14.2 μJy beam*$^{-1}$*. Contours of the* sub-mm map *are drawn at 4, 6, 7, 9, 10, 11 & 11.5 mJy beam*$^{-1}$*. The positions of the radio sources and relevant objects in the NIR (see Fig. 1), are plotted for reference. The black circle inside the box in the bottom-right corner is the beam size of the sub-mm map (*15″ × 15″*), whereas the white one (almost covered by the black circle) corresponds to the beam size of the radio map (*15.06″ × 14.26″*, in position angle* PA = 68.3°*).*

3.4 Comparison of the radio, sub-mm & optical/NIR data

3.4.1 Sub-mm vs Radio emission: morphology and flux density ratio

Figure 3.3 presents the sub-mm and tapered radio maps with a common resolution of ∼ 15″ × 15″. The regions of radio and sub-mm emission are not only coincident, but they are extended on the same angular scale (∼ 1′) and have a strikingly similar morphology. This strongly suggests that the radio and sub-mm emission are associated with each other and are produced by the same (lensed) sources, probably star forming galaxies at $z > 2$. In addition, the positions of the radio components located at *Rb1*, *Rb2*, *Rc1*, *Rc2* and *Fa* (see Fig. 3.1) are consistent with the sub-mm emission that could not be reproduced using only the ERO images and *ARC1* (see B04).

However, Fig. 3.3 also shows some differences in the morphology of the radio and sub-mm emission. The most relevant one is that the brightest region in sub-mm is not associated with the brightest region in radio (*Rb1/Rb2*), but with the second brightest (*Ra1/Ra2*). One explanation for this apparent discrepancy in *Rb1/Rb2*, is that the radio

Table 3.5: ***Flux density ratios.*** *The columns show: name of the sub-mm emission (SMM), redshift of the sub-mm source (z), cluster in which the sub-mm emission is located (Cluster lens), SED template that provides the best fit to the observed flux ratio (Best SED template), flux density ratio obtained from observations (FDR obs), flux density ratio predicted by the template (FDR temp), deviation between the observed and predicted flux ratio (deviation). The value of* FDR observed *in SMM J16359+6612 was calculated by adding the fluxes of all the images together. The deviations were calculated as* (FDR template / FDR observed)-1.

SMM	z	Cluster lens	SED	FDR obs	FDR temp	deviation	References
J14011+0252	2.56	A1835	NGC5253	127 ± 37	115	-0.09	I01
J16359+6612	2.516	A2218	Mrk231	60 ± 10	49	-0.18	K04; G05
J04542-0301	2.9	MS0451	M82	100 ± 11	115	0.15	Sect. 4.1

and sub-mm emission arise from slightly different regions in the source plane and are differentially magnified. This effect could be quite significant for sources lying close to or extending across a caustic. Indeed, we note that recent Mid-IR and radio studies of local star forming galaxies show variations across the disk of up to a factor of ~ 5 in the ratio of the FIR and radio luminosity (Murphy et al. 2004). Another possibility is that the radio emission in the region *Rb1/Rb2* is not only associated with the sub-mm emission that arises from high-z star formation but from an additional component, perhaps an AGN in the foreground cluster that has no counterpart in the sub-mm. Indeed, a possible galaxy cluster member is located within 1.5″of the radio component *Rb1*, and may be an optical/NIR counterpart to this source (see Table 3.6).

The tapered map (see Fig. 3.3) also shows an extension of the radio emission towards *B3/C3* which is not seen in Fig. 3.1. This suggests the possible existence of an extended radio source in this region, presumably associated with the faint sub-mm emission "toe" that appears in the image presented by B04. This is consistent with the existence of the radio counterpart Rc3 predicted by the lens model.

Assuming that the radio and sub-mm emission is produced by the same galaxies, the $S_{850\mu m}/S_{1.4GHz}$ flux density ratio provides information about their spectral energy distributions (SEDs). Note that, since the sub-mm image does not resolve the radio components shown in Fig. 3.1 due to the poor resolution of SCUBA, the radio flux density should be obtained from the tapered radio map. The integrated flux densities were calculated with the AIPS task TVSTAT, using the 4 mJy beam^{-1} sub-mm contour to delimit the same integration area in the sub-mm and tapered radio maps (see Fig. 3.3). Using this method, we find $S_{850\mu m} = 54.6 \pm 5.7$ mJy and $S_{1.4GHz} = 0.547 \pm 0.03$ mJy. The errors were calculated using the expression $\sigma_{beam} \times \sqrt{N}$, where σ_{beam} is the noise per beam of the image, and N is the number of beams within the area delimited by the 4 mJy beam^{-1} sub-mm contour.

The observed $S_{850\mu m}/S_{1.4GHz}$ flux density ratio in MS0451.6−0305 was compared with the flux density ratio obtained from a set of SED galaxy templates. This set is composed by the archetype star forming galaxies Arp220 and M82 (Polletta et al. in prep), the AGN-dominated galaxy Mrk 231, and the set of Blue Compact Dwarf

galaxy SEDs presented in Hunt & Maiolino (2005). To detect possible differences in the nature of faint and bright sub-mm sources, we also performed the same analysis for the faint sub-mm source detected in A2218, and the bright source detected in A1835 (see Table 3.5).

We find that the observed flux density ratio in MS0451.6−0305 is closer to the one obtained using the SED template of M82. However, we note that the observed total flux ratio is being underestimated due to the "excess" of radio emission associated with *Rb1/Rb2*, and therefore a SED similar to Arp 220 may be more appropriate for this source. Until the sub-mm emission can be resolved into different components to determine their flux ratios independently, all we can conclude is that the overall flux density ratio is largely consistent with the favored hypothesis that the bulk of the radio/sub-mm emission is arising from distant star forming galaxies that appear to follow the well known *FIR-radio correlation* (see page 24).

The bright source in A1835 is the only one which is well fitted by one of the BCD templates presented by Hunt & Maiolino (2005). The faint source in A2218 seems to be similar to Mrk 231, perhaps suggesting it is a "warm" SCUBA source following the classification presented in Egami et al. (2004).

3.4.2 Optical/NIR counterparts to the radio emission

B04 proposed that the sub-mm emission is related with three objects (see Fig. 3.1): A LBG (imaged as *ARC1* and *ARC1 ci*) and a pair of triply-imaged EROs (*B*, imaged as *B1/B2/B3*; and *C*, imaged as *C1/C2/C3*).

As is shown in Fig. 3.1, *ARC1* is situated well inside the region of radio emission associated with *Ra1/Ra2*, and is therefore probably related to it. However, in the case of the ERO pair, the images *B1* and *C1* are located at the edge of the radio emission, suggesting that they are not directly contributing a significant amount of the radio flux density in this region.

On the other hand, as shown in Fig. 3.1, although *ARC1ci* and *TF* (an ERO from T03) are most likely contributing to some of the measured flux density in the "sub-mm toe", *B3/C3* is coincident with the maximum of this region. Therefore the EROs are certainly related to the sub-mm emission, so we expect them to be related with the radio emission as well.

The offsets between the estimated centres of the radio emission and the optical/NIR candidates in the image plane are summarized in Table 3.6. Note that the offsets of *ARC1* and the ERO images with respect to *Ra1* and *Ra2* are larger in declination (ΔDEC = 3″) than in right ascension (ΔRA = 2″). This is probably an effect of the magnification produced by the lens cluster, whose largest component is preferentially aligned in the direction of declination (as is reflected in the direction of *ARC1* and the overall morphology of the sub-mm and radio emission). In the source plane, our lens model predicts that the offset between *Ra* and the ERO pair in the image plane is reduced to $\sim$ 1″. Indeed, as shown in Sect. 3.2, the LBG and the EROs probably constitute an interacting system, with the radio source *Ra* situated between them in the source plane. This suggests that the detected radio and sub-mm emission may come from the region in which the systems interact, perhaps due to the enhanced star formation produced by the merging process. A similar phenomena is

Table 3.6: ***Suggested NIR counterparts.*** *The columns show: name of the radio source (Radio Source), name of the suggested NIR counterpart (Counterpart), coordinates of the counterpart source (RA, DEC), offsets between the position of the radio source and its NIR counterpart (ΔRA, ΔDEC) and references that contain information about the counterpart sources (References). Note that ΔRA, ΔDEC should be interpreted as indicative values (see Sect. 3.4.2 for details). The coordinates are given as offsets with respect to the cluster centre,* RA(J2000) = $4^h54^m10.8^s$, DEC(J2000) = $-3°0'51.6''$ *(see Takata et al. 2003, Table 2).*

Radio source	Counterpart	RA ($''$)	DEC ($''$)	ΔRA ($''$)	ΔDEC ($''$)	References
Fb	BCG	1.1	−0.8	2.4	0.0	1
Fd	0451-03C	63.4	−16.2	0.8	1	1
Fe	0451-03A	−21.6	−1.2	0.7	1.1	1
Ra1	ARC1C[1]	32.2	−4.3	1.9	−2.8	2
Ra1	ARC1BE[2]	31.9	−6.3	1.6	−0.8	3, F720W HST image
Ra2	ARC1C[1]	32.2	−4.3	0.8	−3.2	2
Ra2	ARC1TE[3]	32.3	−1.7	0.9	2.8	3, F720W HST image
Ra2	B1	29.8	−0.1	−1.4	−6.4	3
Ra2	C1	30.0	0.1	−1.4	−2.9	3
Ra1	B2	28.5	−9.7	−1.8	2.1	3
Ra1	C2	28.5	−7.5	−1.8	0.4	3
Rb1	Tc	27.9	−24.7	1.4	−1.3	4
Rb1	GCM[4]	24.8	−25.4	−1.8	−0.6	3, F720W HST image
Rb2	Td	20.5	−29.7	−1.8	−0.8	4

Counterpart: (1) AC1 centre; (2) AC1 bottom end; (3) AC1 top end, (4) galaxy cluster member
References: (1) Stocke et al. (1999); (2) C. Borys, private communication; (3) Borys et al. (2004a); (4)Takata et al. (2003)

also observed in the Antennae galaxy, where the bulk of the 20 cm radio emission is situated between the nuclei of both galaxies (see Hummel & van der Hulst 1986). This scenario can explain the offsets between the radio, sub-mm and NIR emission observed in the region of *ARC1*, *B1* and *C1* in the image plane.

Moving to the southern region of Fig. 3.1, the open diamonds correspond to the positions of three additional EROs reported in T03. Two of these EROs (*Tc* and *Td*) are located within 2$''$ of *Rb1* and *Rb2* (see Table 3.6), and may be their NIR counterparts. In this case we expect them to be mirror images, as we assumed in our lens model. We note that Takata et al. argue that these EROs have different photometric redshifts (z_C = 3.730, z_D = 0.5), which is inconsistent with that hypothesis. However, both show the same colors (within the errors) in all bands except for B and I_c, and in those cases the differences may be due to contamination effects (from the galaxy cluster members situated close to *Tc*) and the use of a different aperture in each source (see T03, Table 1). Therefore, with this information we cannot discard the possibility that *Tc* and *Td* are lensed images of the same source. On the other hand, the scenario in which *Tc* and *Td* are not mirror images (but still the optical/NIR counterparts of *Rb1*

and *Rb2*), is also possible within the lensing context. As is shown in Fig. 3.1, *Rb1* is located very close to the critical curve presented in B04, so a small change in its position can move it right on top of the critical curve (and the source component on top of the caustic), resulting in extremely high magnifications. This is consistent with the non-detection of the predicted counterpart image *Rb3*, and the high brightness of *Rb1* in the image plane. We also note that the shape of *Tc* is extremely elongated in the same direction of other faint arcs that appear in the same region of the Hubble image, suggesting that *Tc* may be lensed.

Another possibility (as discussed earlier in Sect. 3.4), is that a possible cluster galaxy member could be the NIR counterpart of *Rb1*. This scenario can also explain the high brightness of *Rb1* if the galaxy cluster member turns out to be a "radio loud" AGN.

Note that four of the six optical/NIR possible counterparts of the radio/sub-mm emission are EROs, which is consistent with the results presented in Knudsen et al. (2005). On the other hand, studies carried out so far are inconclusive with respect to the overlap between LBGs and SMGs (Chapman et al. 2002b; Adelberger et al. 1998; Webb 2002; Huang et al. 2005). However, in the scenario proposed here, the radio and sub-mm emission is the result of an interaction that involves a LBG, rather than emission coming from the LBG directly.

Apart from the effects of lensing magnification, we also identify four other possible sources of error associated with the measured offset positions. In order of importance these include:

- Random measurement errors in the determination of the centre of the unresolved, blended radio components.
- Errors in the choice of the position of *ARC1*, due to its extended and complicated structure.
- Systematic errors due to offsets between the HST and VLA coordinate reference systems (expected to be up to $\sim 1''$, but clearly not dominant since no systematic trend is shown in Table 3.6).
- Intrinsic offsets that can appear if the radio and sub-mm emission come from different regions in the source plane.

Since we cannot properly estimate the contribution of these errors (with the exception of the systematic error), the offsets shown in Table 3.6 should be taken as indicative values.

3.5 Summary and Conclusions

We have presented deep VLA archive observations at 1.4 GHz of the central region of the cluster MS0451.6−0305, discovering multiply-imaged radio sources coincident with the sub-mm emission SMM J04542−0301, originally discovered by Chapman et al. (2002a) and recently studied by Borys et al. (2004a). This is the second case of multiply-lensed radio emission coming from an intrinsically faint SMG (the first case

was SMM J16359+6612 in A2218, see Kneib et al. 2004b; Garrett et al. 2005).

With a resolution of $7'' \times 6''$, the radio emission associated with SMM J0452−0301 can best be represented by seven discrete Gaussian components. A simple lens model of this system (based on a NFW mass profile) can reproduce the positions of the radio components assuming that they are multiple images of 3 background sources located at z = 2.9. However, the model raises some questions that need to be resolved.

Although the radio and sub-mm emission are clearly coincident and present a similar and unusually large angular extent (~1′) and morphology (as expected if the radio and sub-mm emission comes from the same sources), the brightest peak of the radio emission is not coincident with the peak in the sub-mm. We find two possible scenarios that might explain this result:

- The discrepancy is due to differential magnification produced by the gravitational lensing effect – assuming that the radio and sub-mm emission have different morphologies and arise from different regions of the galaxy. Indeed, we note that *Rb1* is situated very close to the critical curve presented in Borys et al. (2004a) (see Fig. 1).

- Part of the radio emission observed in that region is produced by an AGN that might be associated with the foreground cluster.

Borys et al. suggested that the sub-mm emission arises from an interacting system of galaxies formed by an ERO pair and a LBG. Although the association of the EROs with the radio emission appears to be uncertain in the image plane (*B1* and *C1* are clearly located at the very edge of the radio emission), one of the three radio sources predicted by our lens model (*Ra*) is situated between the LBG and the ERO pair in the source plane. Our interpretation of this result is that the interacting region of the LBG and the ERO pair might be the source of the radio and sub-mm emission (due to the intense star formation generated during the merging process), whereas the optical/NIR emission might correspond to the cores of the merging galaxies. This scenario (a situation already observed e.g. in the Antennae galaxy) provides a consistent explanation of the offsets between the radio, sub-mm and NIR emission observed in the image plane (upper region of the map).

From the analysis presented in Borys et al. (2004a), it is also evident that the LBG and the ERO pair cannot account for all the emission coming from the central region of the sub-mm map. However, the higher resolution VLA observations show extended radio emission located in that region, which is expected to arise from 2 radio sources. Two of the components of that extended emission (*Rb1* and *Rb2*) could be related with another two EROs discovered by Takata et al. (2003) (*Tc* and *Td*). Both EROs show similar colors, supporting the idea (assumed in our lens model) that *Rb1* and *Rb2* are images of the same source. However, this latter scenario implies that the photometric redshifts of *Tc* and *Td* reported in Takata et al. (2003) may be incorrect. We also found a bright galaxy (probably a cluster member) that can be the optical/NIR counterpart of *Rb1*, keeping open the possibility that this particular region of

the radio map might include emission from a foreground AGN. Unfortunately, none of the evidence is compelling enough to discriminate between the various scenarios that might explain the nature of *Rb1* and *Rb2*.

In summary, we conclude that the radio and sub-mm emission found in the core of the cluster MS0451.6−0305 arises from at least 3 highly magnified background sources, one of them being the interacting system proposed by Borys et al. (2004a).

Further progress with this system requires a more complete comparison of multi-wavelength data to be made, and a more detailed lens model to be constructed. Deep, mid-IR observations, as well as higher resolution sub-mm data, might be very important in understanding this system, in particular to confirm the possible lensed nature of *Rb1* and *Rb2*.

Acknowledgments

The authors would like to thank Colin Borys for providing us with the HST/SCUBA reduced images and the contours of the lens model presented in his paper to prepare and analyze our figures. We also want to thank James Bullock for providing us his code to estimate the concentration parameter expected for MS0451.6−0305, Charles Keeton for helping to solve problems with the GRAVLENS code, Andy Biggs for his assistance during the data reduction, Antonio Hernán Caballero and Leslie Hunt for providing us with the SED templates, and John Stockes for answering questions related to the bright sources in the field. The authors are also very grateful to the referee for his/her constructive comments which helped to greatly improve the overall manuscript. ABA is also grateful to Edo Loenen for very valuable comments, suggestions and help during the writing of the manuscript. This work was supported by the European Community's Sixth Framework Marie Curie Research Training Network Programme, Contract No. MRTN-CT-2004-505183 "ANGLES".

3.A Calculation of the concentration parameter and the virial mass of the cluster

The NFW density profile (Navarro et al. 1996) is defined in the three-dimensional space as:

$$\rho(r) = \frac{\rho_s}{(r/r_s)(1 + r/r_s)^2} \tag{3.1}$$

where ρ_s is the characteristic density and r_s is the scale radius.

However, the GRAVLENS code (Keeton 2001) works with the projected surface mass density of the NFW profile, which is given by:

$$\kappa(r) = 2\kappa_s \frac{1 - \mathcal{F}}{x^2 - 1}\ ; \qquad \kappa_s = \rho_s r_s / \Sigma_{\rm crit} \tag{3.2}$$

where $x = r/r_s$, κ_s is the mass scale, and $\mathcal{F}$ is defined as:

$$\mathcal{F}(x) = \begin{cases} \frac{1}{\sqrt{x^2-1}} \tan^{-1} \sqrt{x^2 - 1} & (x > 1) \\ \frac{1}{\sqrt{1-x^2}} \tanh^{-1} \sqrt{1 - x^2} & (x < 1) \\ 1 & (x = 1) \end{cases}$$

Following the formalism used in Bullock et al. (2001), we define the scale radius as:

$$r_s = R_{\rm vir}/c_{\rm vir} \tag{3.3}$$

where $c_{\rm vir}$ is the concentration parameter and $R_{\rm vir}$ is the virial radius.

Comparing the definitions of virial mass used in Navarro et al. (1996) (M_{200}) and Bullock et al. (2001) ($M_{\rm vir}$), the characteristic density can be written as:

$$\rho_s = \rho_u(z)\ \delta_c \tag{3.4}$$

where ρ_u(z) is the universal density at redshift z, and δ_c is the characteristic over-density, which is linked with $c_{\rm vir}$ by the following expression:

$$\delta_c = \frac{\Delta_{\rm vir}(z)}{3} f(c_{\rm vir})$$
$$f(c_{\rm vir}) = \frac{c_{\rm vir}^3}{\log(1+c_{\rm vir}) - \frac{c_{\rm vir}}{1+c_{\rm vir}}}$$

The parameter $\Delta_{\rm vir}(z)$ is called the virial over-density, and can be approximated (Bryan & Norman 1998) by:

$$\Delta_{\rm vir}(z) \simeq (18\pi^2 + 82x - 39x^2)/\Omega_m(z) - 1$$
$$x = \Omega_m(z) - 1$$

Combining equations 3.1, 3.2, 3.3 and 3.4, the concentration parameter can be calculated using the following expression:

$$f(c_{\rm vir}) = \frac{3\ \kappa_s\ \Sigma_{\rm crit}}{\rho_u(z_{\rm cl})\ r_s\ \Delta_{\rm vir}(z_{\rm cl})} \tag{3.5}$$

The terms κ_s and r_s are given by the lens model (see Table 3.4). Using the estimated redshift of MS0451.6−0305 from Luppino et al. (1999) ($z_{\rm cluster} = 0.55$), $\rho_u(z_{\rm cluster})$ was calculated scaling the value for z = 0 given in Bullock et al. (2001) ($\rho_u(z = 0) = 8.3 \times 10^{10} h^2$ $M_\odot$ Mpc^{-3}).

Finally, knowing the value of c_{vir}, the virial mass of the cluster can then be estimated as:

$$M_{\rm vir} = \frac{4\,\pi}{3} \Delta_{\rm vir}(z_{\rm cl})\, \rho_{\rm u}(z_{\rm cl})\, R^3_{\rm vir} \tag{3.6}$$